Received: 11 June 2023 | Revised: 20 December 2023 | Accepted: 22 December 2023

DOI: 10.1002/mp.16936

RESEARCH ARTICLE

MEDICAL PHYSICS

Towards optimal heterogeneous prostate radiotherapy dose prescriptions based on patient-specific or population-based biological features

Yutong Zhao[1] | **Annette Haworth**[2] | **Hayley M. Reynolds**[3] | **Scott G. Williams**[4,5] | **Robert Finnegan**[2,6,7] | **Pejman Rowshanfarzad**[1] | **Martin A. Ebert**[1,8,9]

[1]School of Physics, Mathematics and Computing, The University of Western Australia, Crawley, Western Australia, Australia

[2]Institute of Medical Physics, School of Physics, The University of Sydney, Camperdown, New South Wales, Australia

[3]Auckland Bioengineering Institute, University of Auckland, Auckland, New Zealand

[4]Sir Peter MacCallum Department of Oncology, University of Melbourne, Melbourne, Victoria, Australia

[5]Division of Radiation Oncology and Cancer Imaging, Peter MacCallum Cancer Centre, Melbourne, Victoria, Australia

[6]Northern Sydney Cancer Centre, Royal North Shore Hospital, St Leonards, New South Wales, Australia

[7]Ingham Institute for Applied Medical Research, Liverpool, New South Wales, Australia

[8]Department of Radiation Oncology, Sir Charles Gairdner Hospital, Nedlands, Western Australia, Australia

[9]5D Clinics, Claremont, Western Australia, Australia

Correspondence
Yutong Zhao, School of Physics, Mathematics and Computing, University of Western Australia, Crawley, Western Australia, Australia.
Email: yutong.zhao960314@gmail.com

Abstract

Background: Escalation of prescribed dose in prostate cancer (PCa) radiotherapy enables improvement in tumor control at the expense of increased toxicity. Opportunities for reduction of treatment toxicity may emerge if more efficient dose escalation can be achieved by redistributing the prescribed dose distribution according to the known heterogeneous, spatially-varying characteristics of the disease.

Purpose: To examine the potential benefits, limitations and characteristics of heterogeneous boost dose redistribution in PCa radiotherapy based on patient-specific and population-based spatial maps of tumor biological features.

Method: High-resolution prostate histology images, from a cohort of 63 patients, annotated with tumor location and grade, provided patient-specific "maps" and a population-based "atlas" of cell density and tumor probability. Dose prescriptions were derived for each patient based on a heterogeneous redistribution of the boost dose to the intraprostatic lesions, with the prescription maximizing patient tumor control probability (TCP). The impact on TCP was assessed under scenarios where the distribution of population-based biological data was ignored, partially included, or fully included in prescription generation. Heterogeneous dose prescriptions were generated for three combinations of maps and atlas, and for conventional fractionation (CF), extreme hypo-fractionation (EH), moderate hypo-fractionation (MH), and whole Pelvic RT + SBRT Boost (WPRT + SBRT). The predicted efficacy of the heterogeneous prescriptions was compared with equivalent homogeneous dose prescriptions.

Results: TCPs for heterogeneous dose prescriptions were generally higher than those for homogeneous dose prescriptions. TCP escalation by heterogeneous dose prescription was the largest for CF. When only using population-based atlas data, the generated heterogeneous dose prescriptions of 55 to 58 patients (out of 63) had a higher TCP than for the corresponding homogeneous dose prescriptions. The TCPs of the heterogeneous dose prescriptions generated with the population-based atlas and tumor probability maps did not differ significantly from those using patient-specific biological information. The generated heterogeneous dose prescriptions achieved significantly higher TCP than homogeneous dose prescriptions in the posterior section of the prostate.

Conclusion: Heterogeneous dose prescriptions generated via biologically-optimized dose redistribution can produce higher TCP than the homogeneous dose prescriptions for the majority of the patients in the studied cohort. For scenarios where patient-specific biological information was unavailable or partially available, the generated heterogeneous dose prescriptions can still achieve TCP improvement relative to homogeneous dose prescriptions.

KEYWORDS
biologically-optimized prescriptions, heterogeneous prostate boost, prostate cancer

1 | INTRODUCTION

Improved biochemical progression-free survival (bPFS) through radiotherapy dose escalation has been reported for multiple phase 3 randomized controlled prostate cancer (PCa) trials.[1–5] Across varying fractionation schedules, including conventional fractionation (CF),[6–8] extreme hypo-fractionation (EH),[9–11] and moderate hypo-fractionation (MH),[12,13] improved tumor control has been observed with escalating dose. However, with increases in the delivery of total energy to the prostate, a rising late Grade ≥ 3 toxicity rate has been observed.[3,10,11,13]This suggests that increasing the dose in order to improve a patient's tumor control risks an increase in severe GU and GI late effects, and that risk provides an upper limit to the energy that can be safely delivered in pursuit of tumor control. As such, without increasing that energy through further dose escalation, a more effective strategy could be the optimal redistribution of the delivered energy according to the spatial distribution of prostate biological features. In the previous research of Her et al.,[14] biologically targeted radiation therapy (BiRT) was introduced whereby the optimal redistribution of dose according to patient-specific cell density distributions for five patients was determined for intensity-modulated radiotherapy (IMRT).[14] This work was later extended for a 63 patient cohort, and a cell density distribution, tumor location probability and grading of intra-prostatic lesions derived from prostate histology data was used to yield the optimal voxel-level dose distributions to guide the generation of treatment plans.[15]

In a clinical situation, spatial maps of tumor characteristics derived from histology data, as used by Her et al.[14] and Zhao et al.,[15] cannot be obtained prior to optimal dose distribution generation. Machine learning estimates based on multi-parametric MRI (mpMRI) data can be used to estimate the data in vivo.[16] However, the accuracy of applying these models may be limited when scanning parameters vary from those used to generate the predictive model. In such cases, the authors hypothesize that population-based data may be used to represent the likelihood of the disease having specific characteristics at each point throughout the prostate gland, or enhance the reliability of patient-specific imaging-derived estimates. By summarizing the voxel-wise histology data of a 63-patient cohort, a statistical biological model (biological atlas) was created by Finnegan et al.,[17] representing the voxel-wise three-dimensional (3D) histology data distribution based on probability distributions for the cohort.

By incorporating the work conducted by Finnegan et al.,[17] this research aimed to further expand the studies of Her et al.[14] and Zhao et al.[15] to generate optimal dose prescriptions without, or partially with, the distribution of population histology data using four fractionation schedules for whole prostate gland radiotherapy. Heterogeneous dose prescriptions were generated and compared with spatially homogeneous prescriptions as well as heterogeneous prescriptions generated via precision (i.e., patient-specific) histology data.

2 | METHODS

2.1 | Data preparation

This study used annotated whole-mount histology data from 63 PCa patients, who were scheduled for routine radical prostatectomy and recruited to a Human Research Ethics Committee approved project (HREC/15/PMCC/125) at the Peter MacCallum Cancer Centre (Melbourne, Australia). The characteristics of this patient cohort are summarized in Table 1.

The methodology for data extraction and processing has already been described in detail in a previous publication.[15] In summary, by processing digitized whole mount prostate histology slides,[18] tumor annotation masks of 9 Gleason Scores (GS) (2 + 2, 3 + 2, 3 + 3, 3 + 4, 4 + 3, 4 + 4, 4 + 5, 5 + 4, 5 + 5)[18] and cell density maps (CD-maps) indicating area cell density distributions[19] were prepared for all patients in the cohort. To generate a 3D volume, the histology slides, which were obtained 5.0 mm apart, were co-registered with corresponding ex vivo T2 weighted (T2w) MRI of the prostate specimens which had 2.5 mm axial slice thickness, and linear interpolation was applied to generate the missing histology data from the CD-maps and

TABLE 1 Summary of patient characteristics.

Clinical characteristics	
No. of subjects (*n*)	63
Mean age in years (SD[a])	62.3 (7.7)
Mean PSA[b] (SD) [ng/mL]	8.9 (6.6)
Risk stratification, number (%) [NCCN[c] risk classification]	
Low-risk	4 (6.3%)
Intermediate-risk	51 (81.0%)
High-risk	8 (12.7%)
Pathological T stage (AJCC[d]/UICC[e] 8th edition)	
T2	31 (49.2%)
T3	32 (50.8%)
Dominant nodule GS[f] (ISUP[g] 2014)	
6	4 (6.3%)
7	53 (84.1%)
≥8	6 (9.5%)

[a]SD: Standard deviation.
[b]PSA: Prostate specific antigen.
[c]NCCN: National Comprehensive Cancer Network (NCCN) risk classification.
[d]AJCC: American Joint Committee on Cancer.
[e]UICC: Union for International Cancer Control.
[f]GS: Gleason Score, which represents the likelihood of tumor aggressiveness.
[g]ISUP: International Society of Urological Pathology.

tumor annotation masks.[17] Consequently, every voxel of each GS of the tumor annotation mask was assigned a probabilistic value (between 0 to 1). When all 9 tumors annotation masks were summed for each patient, a tumor probability map (TP-map) was produced, containing voxel-wise likelihoods of the presence of tumor cells. The 2D CD-maps were raised to the power of 3/2 to convert to the volumetric cell density distribution.[17] Finally, the resulting CD-maps and TP-maps were resampled to the same isotropic resolution of $0.8 \times 0.8 \times 0.8$ mm^3.

With using the same 63-patient cohort, the population-based statistical cell density and tumor probability distributions (the biological atlas) was built using these data, and is described in detail by Finnegan et al.[17] In summary CD- and TP-maps of each individual in the cohort were deformably registered to a common reference geometry. The cell density and tumor probability distributions for each voxel were fitted to log-normal and linear-normal models, respectively. This resulted in a reference prostate geometry containing voxel-wise population-based distributions of cell density and tumor probability, referred to in this report as the cell density atlas (CD-atlas) and tumor probability atlas (TP-atlas) respectively.

The atlas information was used in this study to supplement the maps for each individual patient. As shown in Figure 1 (TP-map (Patient)), since TP-maps only contain voxel-wise tumor probability for voxels encompassed by annotated tumors, the tumor probability for the remaining prostate volume was assigned a probability of 0%. Hence, to complete the distribution of tumor probability for the entire prostate in the TP-map, voxels with tumor probability values lower than the corresponding mean tumor probability of the population (TP (patient + atlas)-map) were replaced by the TP-atlas indicated mean tumor probability. The procedures for generating CD-maps, TP-maps, CD-atlas, and TP-atlas are summarized in Figure 2.

2.2 | TCP model

The cell density indicated from both the CD-map and CD-atlas includes both tumor cells and healthy cells. Tumor cell numbers therefore had to be estimated. When a voxel, i, was defined as tumor, its tumor cell number N_i could be estimated through:

$$N_i = A_{risk} \cdot \rho_i \cdot V$$

where the product of total cell density ρ_i and voxel volume V gives the total cell number (including both normal and cancer cells) of the voxel i. The normalization factor, A_{risk}, is used to linearly scale the total cell number to match the corresponding median tumor cell numbers in each risk group as estimated by Wang et al.[20] A_{risk} can be interpreted as the percentage of the tumor cells in a voxel.

To determine optimal dose distributions, a linear-quadratic (LQ) tumor control probability (TCP) model was used as an objective function, incorporating a truncated log-normally distributed radiosensitivity distribution.[14,15,21,22] For the i^{th} voxel, with tumor cell number N_i and tumor probability TP_i given by constant values (i.e., sampling by distribution is not required), the TCP_i was determined using the calculated total tumor cell number N_i, a value of $\frac{\alpha}{\beta}$ of 3.1, the total number of treatment fractions n, the dose per fraction d_i, overall treatment duration T_{exp}, and the potential doubling time T_{pot} of 42 days,[20] according to the reports by Shusharina et al.[23] and Bortfeld et al.[24]:

$$TCP_i\,(N_i, \alpha_k, d_i, TP_i) = exp\left[-N_i \exp\left(-\alpha_k n d_i - \frac{\alpha_k n d_i^2}{\frac{\alpha}{\beta}} + ln\,(2)\,\frac{T_{exp}}{T_{pot}}\right)\right] \cdot TP_i + (1 - TP_i) \quad \alpha_k \epsilon\,[0.05, 0.4] \tag{1}$$

It was assumed that α_k follows a log-normal distribution[21,25] defined by a mean value $\bar{\alpha}$ and a standard deviation σ_α, with $\bar{\alpha} = 0.15\ Gy^{-1}$ and $\sigma_\alpha = 0.04\ Gy^{-1}$,[20] and sampled in the interval of $0.05 \leq \alpha_k \leq 0.40$. Therefore, the TCP value of the entire

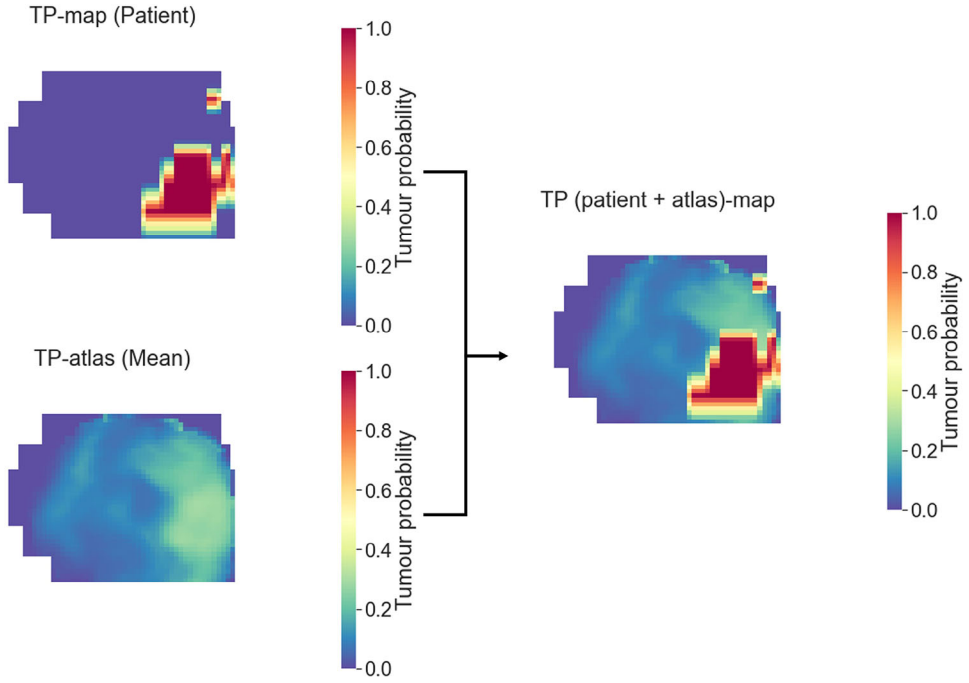

FIGURE 1 Tumor probability distribution in the coronal plane of the prostate. Combining the tumor probability distribution of annotated tumors (TP-map (Patient)) and that of the population average (TP-atlas (Mean)), resulted in the tumor probability distribution for the entire prostate (TP (patient + atlas)-map).

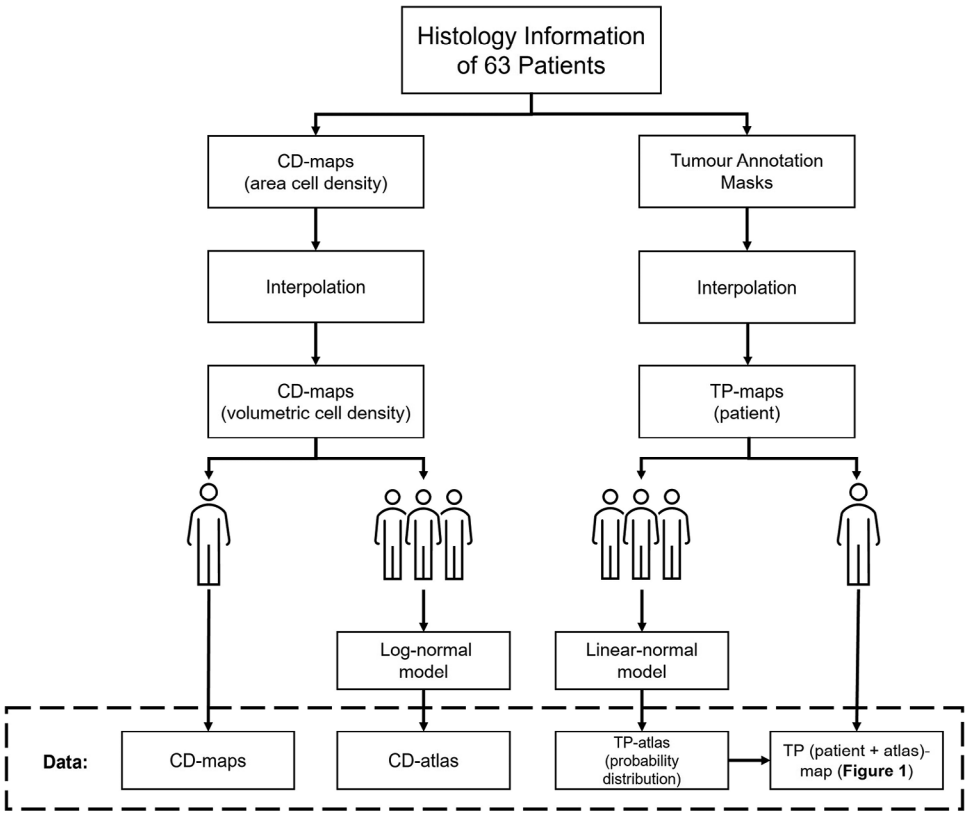

FIGURE 2 Schematic overview of the pipeline for generation of the maps and atlas used in this study. Note that the CD- and TP-maps represent each individual's CD and TP distribution, whereas the CD- and TP-atlas combine the CD and TP distribution of the population of patients, and the TP (patient + atlas)-maps were the combined tumor probability distributions of TP-atlas and individual's TP-maps.

prostate gland (with total M voxels) with sampled α_k was calculated as the product over all individual voxels:

$$TCP(\alpha_k) = \prod_{i=1}^{M} TCP_i(N_i, \alpha_k, d_i, TP_i) \quad \alpha_k \epsilon [0.05, 0.4] \tag{2}$$

The weighting factors, $\omega(\alpha_k)$, of the corresponding $TCP(\alpha_k)$ were obtained from the normalized probability density of the log-normal distribution, and the overall TCP was calculated by weighting and averaging all $TCP(\alpha_k)$ values.

$$TCP = \frac{1}{W} \sum_{k=1}^{H} \omega(\alpha_k)\, TCP(\alpha_k) \quad \alpha_k \epsilon [0.05, 0.4] \tag{3}$$

When the TCP was calculated with a log-normal distributed cell density as provided by the CD-atlas, with sampled cell density values, and therefore calculated tumor cell number $N_{i,M}$, the TCP of the i^{th} voxel was computed via:

$$\begin{aligned} &TCP_i\left(N_{i,M}, \alpha_k, d_i, TP_i\right) \\ &= exp\left[-N_{i,M} \exp\left(-\alpha_k n d_i - \frac{\alpha_k n d_i^2}{\frac{\alpha}{\beta}} + ln(2)\frac{T_{exp}}{T_{pot}}\right)\right] \\ &\cdot TP_i + (1 - TP_i) \quad \alpha_k \epsilon [0.05, 0.4] \end{aligned} \tag{4}$$

Then, with the weighting factor $\omega(N_{i,M})$, taken from the probability density of the voxel-level cell density log-normal distribution, and the U sampled $N_{i,M}$, the overall TCP of the i^{th} voxel was computed via:

$$\begin{aligned} &TCP_i\left(N_{i,M}, \alpha_k\right) \\ &= \frac{1}{\sum \omega\left(N_{i,M}\right)} \sum_{M=1}^{U} \omega\left(N_{i,M}\right) TCP_i\left(N_{i,M}, \alpha_k, d_i, TP_i\right) \end{aligned} \tag{5}$$

Hence, the TCP value of the entire prostate gland with sampled α_k could be calculated as:

$$TCP(\alpha_k) = \prod_{i=1}^{M} TCP_i\left(N_{i,M}, \alpha_k\right) \quad \alpha_k \epsilon [0.05, 0.4] \tag{6}$$

To expedite calculation when the TP-atlas was used for TCP calculation, the mean of the linear-normal distributed tumor probability from the TP-atlas was used, rather than a full sampling of the full distribution.

2.3 | Prescription generation

It was assumed that redistribution of energy within the target would have minimal impact on dose distributions to adjacent healthy structures. The prescribed dose distributions, representing optimal dose distributions, were generated through maximization of total TCP under the constraint of a fixed integral deposited energy, E. As a result, for practical purposes, for the same patient and fractionation schedule, all generated prescriptions were obtained through redistribution of the identical integral energy level, E, calculated using the mass m_i of all voxels incorporating the dose distribution and the average dose level D_{ave}.

$$E = \sum_{i=1}^{M} E_i = \sum_{i=1}^{M} D_{ave} \cdot m_i \tag{7}$$

The CD- and TP-atlas were deformably registered with each patient-specific prostate geometry using the inverse transform computed during atlas construction. This provided each patient with two sets of spatial tumor characterizations—their CD- and TP (patient + atlas)-map representing the patient-specific distribution of biological features, and the CD- and TP-atlas representing the population-based distribution of biological features. Each of these sets of characteristics were combined in various ways to generate four different methods of heterogeneous dose prescription to adapt four clinical scenarios. A schematic overview is shown in Figure 3:

1. Method-1 [Uniform distribution, no patient-specific or atlas information used]: By ignoring the atlas and patient-specific biological information and assuming a homogeneous distribution of prostate biological characteristics, the Method-1 prescription represents a uniform dose distribution across the entire prostate. This represents the "conventional" approach to dose prescription.
2. Method-2 [CD-atlas + TP-atlas, no patient-specific information used]: The prescriptions of Method-2 were generated by incorporating population-based biological distributions from the CD- and TP-atlas. This represents a situation where no patient-specific information is available.
3. Method-3 [CD-atlas + TP (patient + atlas)-map, partially patient-specific information used]: Prescriptions were generated using population-based cell density information from the CD-atlas and each individual's tumor probability distribution from their TP (patient + atlas)-map. This represents the situation where the TP (patient + atlas)-map can be derived from TP-atlas and the locations of IPLs that were identified by annotated medical images (e.g., annotated

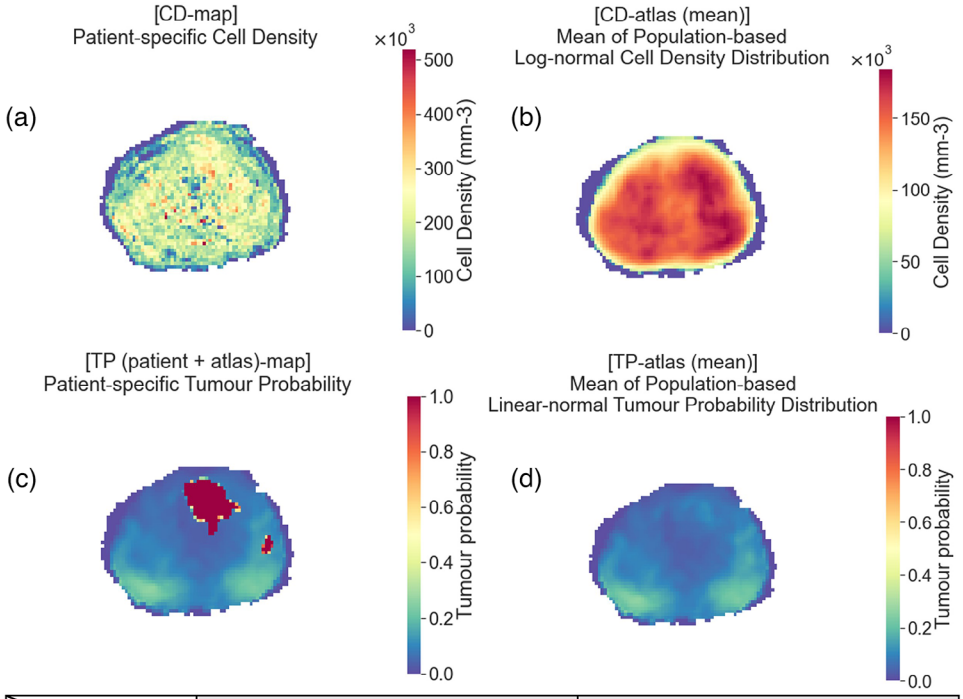

	Cell Density Distribution		Tumour Probability Distribution	
	CD-atlas	CD-map	TP-atlas	TP-map (Patient)
Method-1	Uniform cell density distribution		Uniform tumour probability distribution	
Method-2	✓		✓	
Method-3	✓		✓	✓
Method-4		✓	✓	✓

FIGURE 3 For a sample patient and the same transverse plane of the prostate, visualized voxel-wise distribution of: (a): cell density indicated by the patient's CD-map, (b): mean cell density calculated from the CD-atlas, (c): tumor probability indicated by the patient's TP (patient + atlas)-map, and (d): mean tumor probability calculated from the TP-atlas. The table provides the distributions of biological features that were used in prescription generation at each Method.

CT, informed by mp-MRI), and assuming no patient-specific cell density information is available.

4. Method-4 [CD-map + TP (patient + atlas)-map, full patient-specific information used]: Assuming full knowledge of the distribution of patient-specific biological features, the Method-4 prescriptions were generated through dose redistribution using each individual's cell density and tumor probability information.

Four fractionation schedules (EH, MH, CF, and whole pelvic radiotherapy (WPRT) + SBRT boost) were considered. The number of fractions, total treatment duration (T_{exp}), average dose level, maximum and minimum doses allowed during dose redistribution are described in Table 2. Average dose refers to the mean dose to the entire prostate and is equivalent to the dose prescribed for the Method-1 (homogeneous) prescription. It is equal to the dose when redistributed during heterogeneous prescription generation.

WPRT + SBRT consists of 25 fractions of 1.8 Gy WPRT and 3 fractions of 10 Gy prostate (only) SBRT. We acknowledge the prescription of WPRT is controversial in PCa radiotherapy, therefore only doses prescribed in the SBRT boost were considered for redistribution in this study, and the impact of WPRT on this study was excluded. The treatment duration of CF and WPRT were estimated by 1.4 times the fraction number.

For the fractionation schedules shown in Table 2, the minimum allowed dose was obtained from the dose level that has commonly been used in conventional radiotherapy with each corresponding fractionation schedule (EH,[10,11,26,27] MH,[12] CF,[28] WPRT + SBRT[29]). The average dose was set to the boost dose reported in studies where a boost dose was prescribed,[30–36] or to the highest dose reported in dose escalation studies.[28] The highest allowed dose was from the maximum prescribed dose in studies that included prostate sub-volume dose escalation (EH and CF[26,37,38]) or 125% of average dose level (MH and WPRT + SBRT).

TABLE 2 Parameters applied in TCP calculation for the four included fractionation schedules.

Schedule name	Extreme hypo-fractionation (EH)	Moderate hypo-fractionation (MH)	Conventional fractionation (CF)	Whole pelvic RT + SBRT boost (WPRT + SBRT)
Fractions	5[26,30–32]	19[33]	45[28]	25 + 3[34–36]
T_{exp} (days)	29[26]	28[12]	1.4 × 45[28]	1.4 × 25 + 6[34,36]
Max. dose (Gy)	50.0 (10.0)[26]	80.75 (4.25)	102.6 (2.3)[37,38]	30.0 (10.0)
Average dose (Gy)	40.0 (8.0)[30–32]	64.6 (3.4)[33]	81 (1.8)[28]	21.0 (7.0)[34–36]
Min. dose (Gy)	35.0 (7.0)[10,11,26,27]	57.0 (3.0)[12]	68.6 (1.5)[28]	18.0 (6.0)[29]

For CF, the average, maximum allowed, and minimum allowed doses were referenced from published PCa fractionation schedules of 81 Gy in 45 fractions, 95 Gy in 35 fractions and 64.8 Gy in 36 fractions. To keep the fraction number of all referenced doses consistent, all referenced fractionation schedules were converted to a 45 fractions treatment schedule under the equivalent biologically effective dose (BED) and for $\frac{\alpha}{\beta}$ of 3.1. The obtained maximum and minimum allowed doses from the corresponding converted treatment schedules are shown in Table 2.

For the 3 fraction SBRT boost in *WPRT + SBRT*, although the defined average dose in this current study was 21 Gy, a more common prescribed dose is 19 Gy[29] or higher (e.g., 19.5 Gy[39,40]). As a larger difference between average and minimum doses allowed for a more heterogeneous dose distribution, the minimum dose allowed was set to 18 Gy.

For each patient in the cohort, a total of 16 optimal dose distributions were generated by finding the voxel-level dose distribution that maximized the corresponding total tumor TCP (i.e., 4 Methods of prescription with 4 fractionation schedules).

The dose redistribution was performed using the metaheuristic differential evolution (DE) algorithm[41,42] from the Python (Python Software Foundation, version 3.8.8) library and math toolkit—SciPy (Community library project, version 1.7.3).[43] To facilitate the optimization process, the redistributed dose distribution was based on a down-sampled 3D cell density (voxel size after down-sampling: 6.4 mm × 6.4 mm × 6.4 mm) and tumor probability distribution.

2.4 | Prescription comparison

To understand the impact of spatial variations in tumor location on optimal TCPs and dose distributions across the gland, the prostate was segmented into 12 sub-sections as shown in Figure 4 and the TCP of each sub-section was calculated and compared for the cohort.

To summarize and compare optimal spatial dose distributions, the expected tumor cell number was calculated for each voxel via the product of their tumor cell number and tumor probability from each patient's CD- and TP (patient + atlas)-map. With voxels ordered by the expected number of tumor cells, the dose of each voxel and for each dose prescription Method were plotted on the same scatter plot for comparison. Method-2 and -3 prescriptions were compared to assess the impact of adding patient-specific tumor probability information. Method-1 and Method-4 prescriptions were compared to assess the TCP improvement achievable using patient-specific biological information. As the Method-4 dose distributions have the potential to achieve the highest possible TCP, the Method-4 dose for each voxel, and each patient, was defined as the reference dose. Doses for each voxel in the Method-1 to -3 dose distributions were compared to the corresponding Method-4 voxel dose.

3 | RESULTS

3.1 | Impact of the prescription and fractionation

3.1.1 | Impact on cohort

Across the whole patient cohort and fractionation schedules, with the patient-specific cell density and tumor probability distribution given by CD-map and TP (patient + atlas)-map, the TCPs of optimized prescriptions for each Method are indicated in Figure 5. The cohort TCP is defined as the product of the TCPs of all patients in each cohort, for each Method across all fractionation schedules. The cohort TCP represent the likelihood of tumor control for all patients. For all fractionation schedules, the average TCPs and cohort TCP increase across prescription Method-1 to -4.

The *P* values of Wilcoxon signed-rank test for resulting optimized TCPs between pairs of prescription Methods were calculated. For all fractionation schedules, the prescriptions of Method-2, -3, and -4 improved the TCP significantly ($p < 0.05$) relative to a uniform dose distribution (Method-1). The TCPs of Method-4 and Method-3 prescriptions were significantly ($p < 0.05$) larger than that of Method-2.

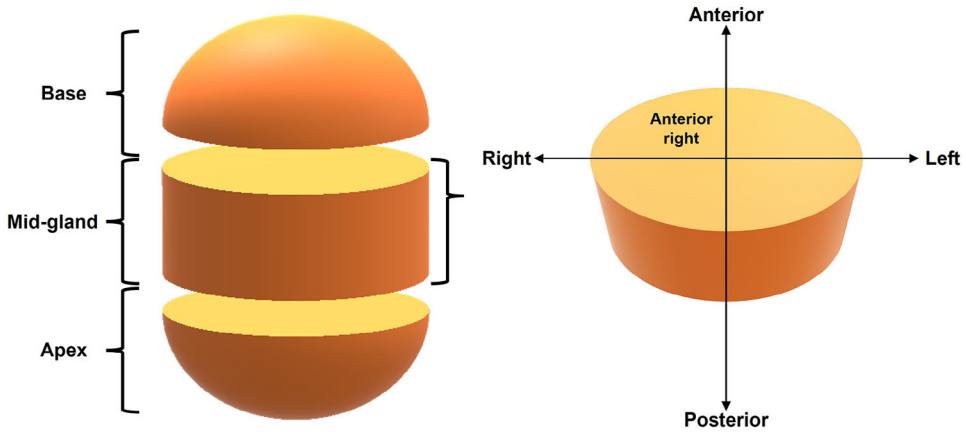

FIGURE 4 Illustration of the prostate segmentation. A total of 12 sub-sections were produced by evenly segmenting the prostate axially into three parts in (apex, mid-gland, and base) and then each part of prostate being further segmented into four sub-sections in the anterior-posterior and right-left directions.

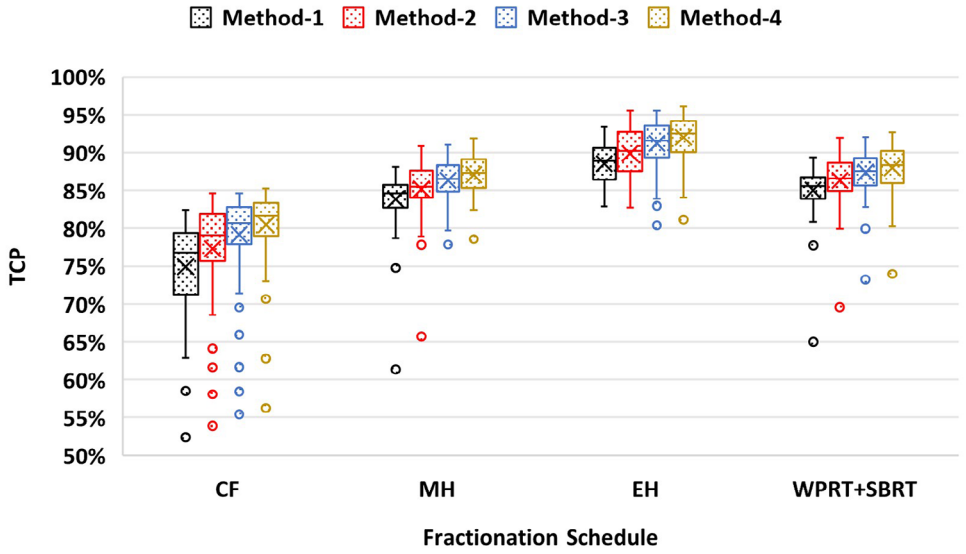

FIGURE 5 TCPs of prescriptions of each Method classified by fractionation schedules are shown in the box plot. *P* values (Wilcoxon signed-rank test) of TCPs of prescriptions for each paired Method are given in the table.

The largest and smallest TCP improvements across the Methods was observed with CF and EH, respectively. Table 3 indicates the number of patients in each cohort experiencing specific changes to TCP when using Method-2 to -4 prescriptions relative to Method-1 prescriptions. As listed in Table 3, the Method-4 prescriptions (generated by full patient-specific information) were able to increase the TCP for all patients in all fractionation schedules, compared to other prescriptions. Most of the cases for which TCP decreased relative to the uniform dose prescription (Method-1) were found amongst the Method-2 prescriptions (generated by population-based information), but the Method-2 prescriptions still achieved higher TCP for at least 87% of patients in MH and EH.

3.1.2 | Impact on individuals

The inclusion of the population atlas in guiding the heterogeneous dose prescription decreased the expected TCP for some patients relative to a conventional uniform dose approach. Figure 6a shows the TCP differences of the Method-2, -3, and -4 prescriptions relative to Method-1 under EH. For 8 patients there was a decrease in TCP for the Method-2 prescription and 1 patient for Method-3. The largest decreases for both Method-2 and -3 prescriptions are seen for patient-07. Figure 6b shows the TCP differences of Method-1, -2, and -3 prescriptions relative to Method-4 under EH. Also relative to the Method-4 prescriptions, the largest TCP difference by Method-2 and -3 prescriptions were also

TABLE 3 The total number of patients with Method-2 to -4 prescriptions which saw TCP increasing or decreasing relative to Method-1 prescriptions.

	CF			MH			EH			WPRT + SBRT		
N	M-2	M-3	M-4	M-2	M-3	M-4	M-2	M-3	M-4	M-2	M-3	M-4
TCP Increased (> = 0%)	56	62	63	55	62	63	55	62	63	58	63	63
High Increase (> = 5%)	6	19	30	0	1	2	0	2	6	0	1	2
Median Increase (> = 1% and < 5%)	46	43	33	40	59	61	40	58	57	37	57	61
Low Increase (< 1%and > = 0%)	4	0	0	15	2	0	15	2	0	21	5	0
TCP Decreased (< = 0%)	7	1	0	8	1	0	8	1	0	5	0	0
High Decrease (< = −5%)	1	1	0	0	0	0	0	0	0	0	0	0
Median Decrease (< = −1% and > −5%)	1	0	0	2	1	0	2	1	0	0	0	0
Low Decrease (> −1%and < = 0%)	5	0	0	6	0	0	6	0	0	5	0	0

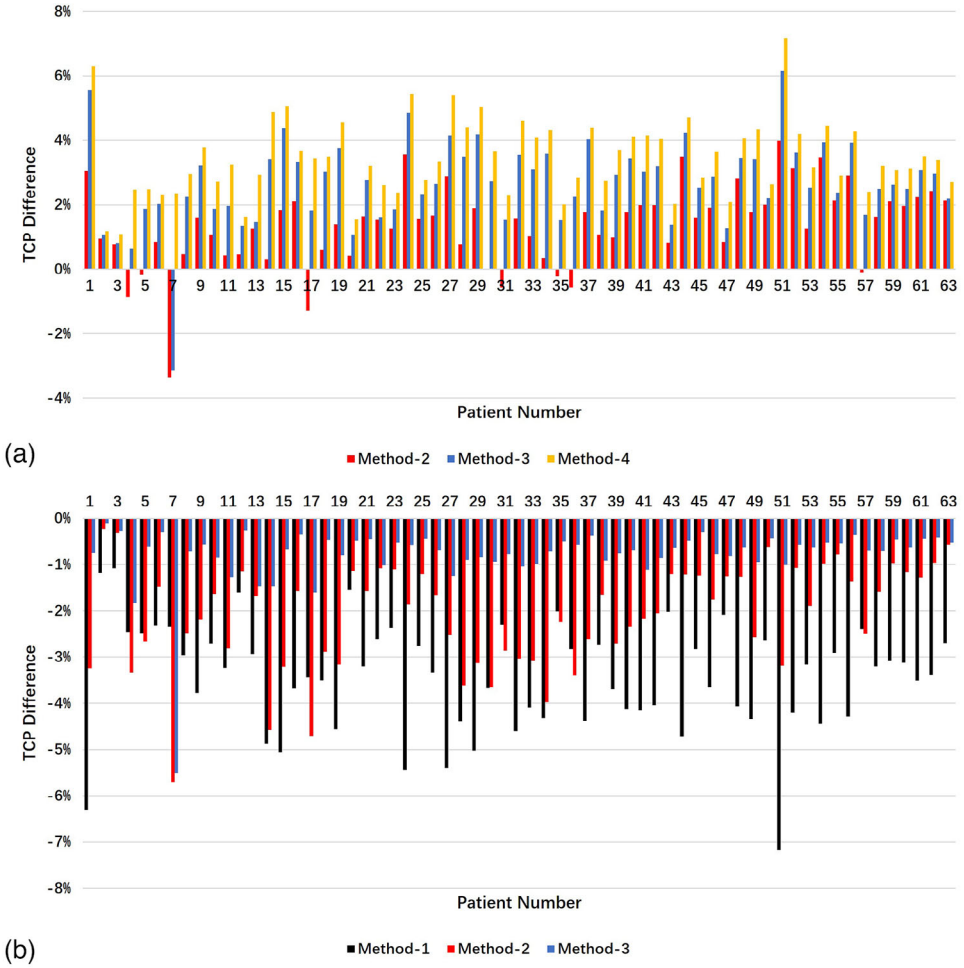

FIGURE 6 For cohort ranked by TCP of Method-4 prescription, the TCP difference of: (a): Method-2, -3, and -4 prescriptions to Method-1 under EH, (b): Method-1, -2, and -3 prescriptions relative to Method-4 under EH.

found for patient-07, while the smallest TCP differences were found for patient-02. For patient-02, the TCPs of Method-1 to -4 prescriptions under EH were 82.86%, 83.81%, 83.94%, and 84.04%, respectively. That for patient-07 were 86.12%, 82.76%, 82.97%, and 88.47%, respectively.

The voxel-wise dose prescription values for 4 Methods under EH for patient-02 and -07 were ranked by expected voxel-wise tumor cell number (product of voxel tumor cell and tumor probability) and shown in Figure 7. The tables below each figure summarize the mean absolute dose difference, the mean voxel doses of

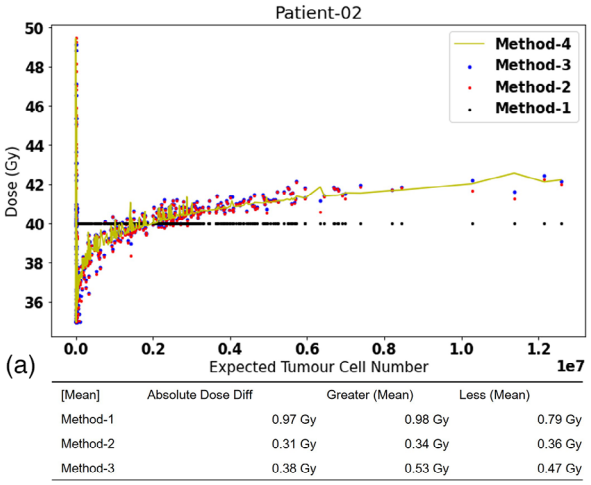

[Mean]	Absolute Dose Diff	Greater (Mean)	Less (Mean)
Method-1	0.97 Gy	0.98 Gy	0.79 Gy
Method-2	0.31 Gy	0.34 Gy	0.36 Gy
Method-3	0.38 Gy	0.53 Gy	0.47 Gy

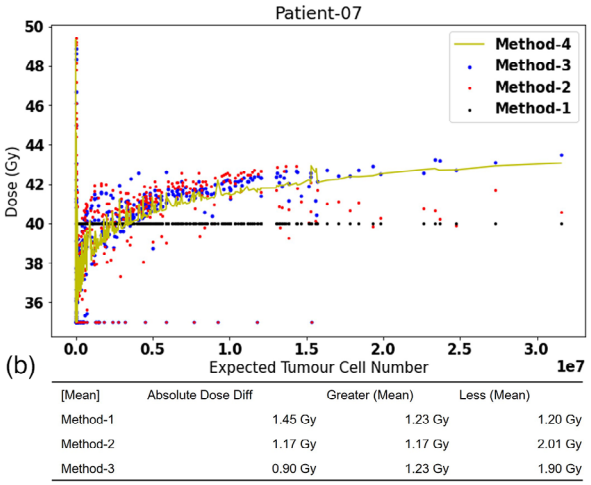

[Mean]	Absolute Dose Diff	Greater (Mean)	Less (Mean)
Method-1	1.45 Gy	1.23 Gy	1.20 Gy
Method-2	1.17 Gy	1.17 Gy	2.01 Gy
Method-3	0.90 Gy	1.23 Gy	1.90 Gy

FIGURE 7 For patient-02: (a) and patient-07: (b), the voxel-wise dose prescription values ranked by expected voxel-wise tumor cell number (product of voxel tumor cells and tumor probability) are plotted. The mean absolute dose levels greater and less than the Method-4 voxel doses are shown in the respective tables.

Method-1 to -3 prescriptions greater than, and less than the Method-4 voxel doses. To find the reported dose difference matrix that most correlated to tumor control, the coefficients of Standard (Pearson) correlation[44,45] were calculated by the reported dose difference matrix (Figure 7) and TCPs of the cohort. For Method-2 and -3 prescriptions, the mean voxel doses less than Method-4 doses had the highest correlation to TCP decreasing (relative to TCP of Method-4 prescription), with a correlation coefficient (CC) of 0.94. The mean absolute dose difference is the second most correlated parameter with a CC of 0.80, and the mean voxel doses greater than Method-4 doses had a CC of 0.36.

3.2 | Variations across prostate zones

For all prescriptions with EH, the TCPs of each subsection of the prostate are visualized in Figure 8. For the entire cohort and each subsection of prostate, Wilcoxon signed-rank test was conducted between TCPs of Method-2 to -4 prescriptions and that of Method-1 prescriptions. The calculated *P* values are listed in Table 4, with values lower than the significant level (0.05) shaded with color. Compared to a uniform dose prescription (Method-1), the Method-2 to -4 prescriptions significantly escalated the local TCP of the entire posterior prostate, and the Method-4 prescriptions also achieved significantly higher TCP in the anterior section of prostate mid-gland.

TABLE 4 *P* values (Wilcoxon signed-rank test) of TCPs between Method-2 to -4 prescriptions and Method-1 prescription in each subsection of prostate for all patients, the values lower than the significant level of 0.05 were shown in bold.

		A-R	A-L	P-R	P-L
Apex	**M-2**	2.2×10^{-1}	5.2×10^{-1}	2.4×10^{-2}	1.0×10^{-3}
	M-3	6.8×10^{-1}	7.6×10^{-1}	1.1×10^{-3}	1.1×10^{-5}
	M-4	9.5×10^{-1}	2.5×10^{-1}	1.0×10^{-4}	2.6×10^{-7}
Mid-gland	**M-2**	9.7×10^{-1}	7.8×10^{-1}	3.5×10^{-5}	1.2×10^{-7}
	M-3	4.2×10^{-1}	2.4×10^{-1}	2.2×10^{-7}	5.3×10^{-10}
	M-4	9.5×10^{-3}	4.8×10^{-3}	1.4×10^{-10}	3.5×10^{-13}
Base	**M-2**	8.8×10^{-2}	3.3×10^{-1}	1.7×10^{-3}	6.2×10^{-4}
	M-3	5.9×10^{-2}	2.4×10^{-1}	2.2×10^{-4}	4.4×10^{-5}
	M-4	5.1×10^{-2}	1.7×10^{-1}	3.9×10^{-5}	1.5×10^{-5}

4 | DISCUSSION

This study developed a mechanism for a voxel-wise optimal dose prescription for the entire prostate gland, under the constraint of total delivered energy, by utilizing biological information derived from prostate histology. Using a TCP model that incorporated voxel-level cell density and tumor probability, the optimal prescriptions were produced in four combinations of CD and tumor probability maps and four fractionation schedules for a total of 63 patients. The impact on optimal TCP was evaluated for prescriptions that incorporated varying inclusion of population-based and/or patient-specific biological information.

4.1 | Prescription generation

The four Methods in this study simulated four scenarios of availability of precision biological information in the clinic. With full knowledge of the patients' histology information, the prescriptions of Method-4 were generated based on precise cell density and tumor probability distributions. However, in clinical practice the full cross-sectional histology data is not available. Hence, in this work we demonstrated that using the delineated IPLs

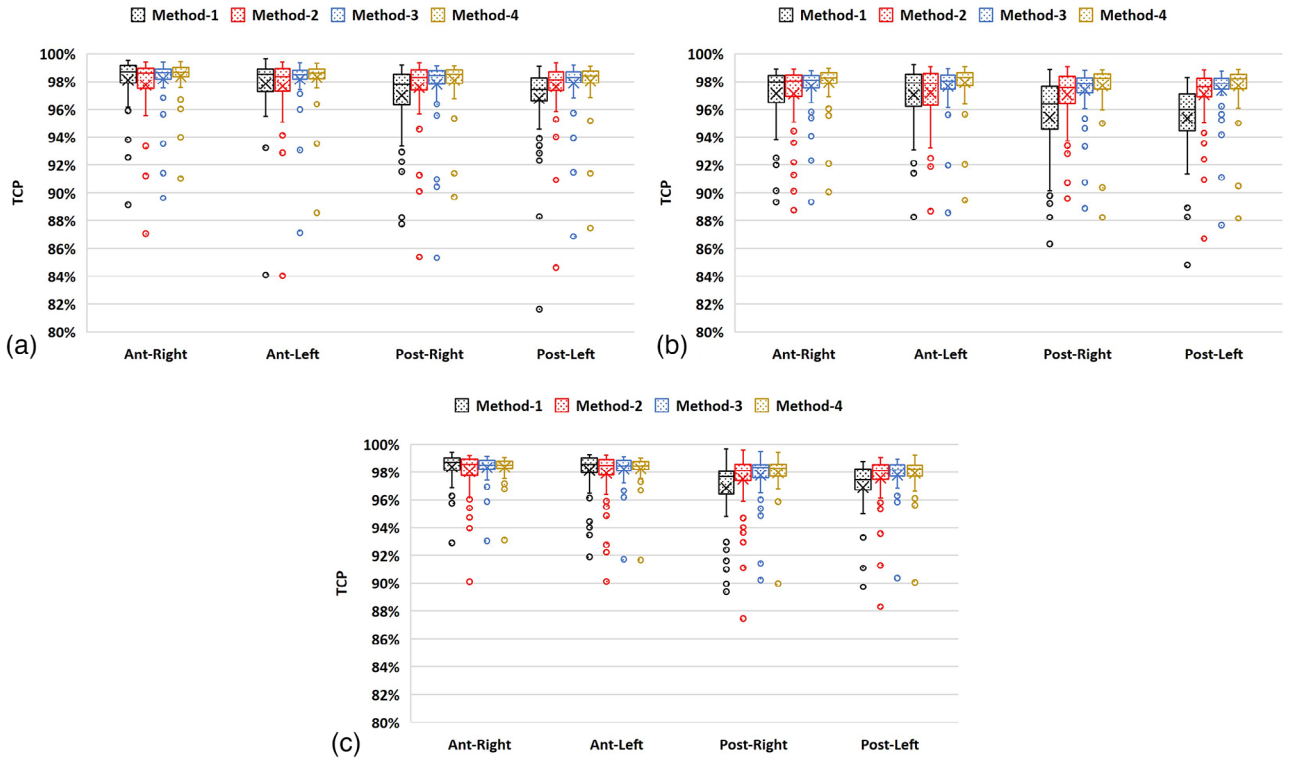

FIGURE 8 TCPs of all 12 sub-sections of prostate for all prescriptions in cohort under EH. (a): Prostate apex. (b): Prostate mid-gland. (c): Prostate base.

on medical images, and the population-based tumor probability of the non-IPL prostate volume indicated by TP-atlas (the Method-3 method) could be used to generate prescriptions by incorporating the population-based cell density distribution from the CD-atlas. Prescriptions for Method-1 and -2 were established to accommodate situations where no patient-specific information was available to support the biological optimization model. The prescriptions generated in Method-1 represent the homogenous dose prescription that is commonly applied in conventional radiotherapy, and Method-2 represents an optimal dose distribution by considering the population-derived distribution of biological features.

It is noticeable that for voxels with expected tumor cell numbers near 0, a high dose was assigned in prescriptions of Method-2 to -4 (Figure 7). As equation (7) indicates, prescriptions in all Methods represented identical integral energy for the same patient and fractionation schedule. For the heterogenous dose prescriptions, the integral energy level can be obtained by the prescribed dose nd_i and mass m_i of all voxels:

$$E = \sum_{i=1}^{M} E_i = \sum_{i=1}^{M} nd_i \cdot m_i$$

The Method-2 to -4 dose distributions had a downsampled 3D size from the original histology data, therefore, the TCPs of each voxel were calculated from the cell density and tumor probability values covered by the corresponding voxel.

When a voxel in the dose distribution is located near the edge of the prostate and covered with a small proportion of prostate tissue and a large proportion of empty volume around the prostate, both expected tumor cell number and the mass of voxel would be very small. The low expected tumor cell number would lead to a high voxel TCP (always near 100%), and the low mass of voxel would result in a low calculated energy of the voxel E_i, $\lim_{m_i \to 0} (nd_i \cdot m_i) = 0$, and E_i can only occupy a minor proportion of total energy E. As a consequence, once the optimizer determined an optimal dose distribution and randomly prescribed a high dose level to those voxels near the edge of the prostate, the optimizer could not further escalate the total TCP above the defined threshold (derived from the defined tolerance in the optimizer) by redistributing the dose for those voxels because they had a TCP near to 100% at any dose level within defined dose range. Additionally, because of the minor proportion to the total energy, the doses prescribed to those voxels were too low to be redistributed to other voxels to escalate total TCP. To address this issue, a lower tolerance could be used by the optimizer and/or the dose distributions could be downsampled by a smaller voxel size. However, both methods increase the computational time. Alternatively, after prescription generation, a mode filter could be implemented to voxels near the edge of

the prostate to prescribe those voxels with the same dose as their neighboring voxels.

4.2 | Impact of the prescription and fractionation

4.2.1 | Impact on cohort

As shown in Figure 5, the average TCP of the cohort for all Methods was the lowest with CF across all fractionation schedules. However, for CF, the average TCP improvements amongst the heterogeneous dose prescriptions (Method-2, -3, and -4) relative to homogenous prescriptions (Method-1) were the largest, and the number of patients who saw high TCP improvement (≥5%) by Method-2 to -4 prescriptions the greatest (Table 3). This indicates, in terms of tumor control, that CF benefited the most from a heterogenous prescription. With EH, MH, and WPRT + SBRT, the TCP improvements of Method-2 to -4 prescriptions relative to homogenous prescriptions were lower than with CF in terms of either range of TCP improvement or the number of benefiting patients. This observation could be explained by the diminishing advantage of heterogeneous dose distributions—when the TCP of the homogeneous prescription is already close to a value of 1. An additional reason for a lower TCP improvement for WPRT + SBRT is that the dose redistribution was only conducted for fractions incorporating an SBRT boost. The prescribed dose distributions in the WPRT part are identical for both homogenous and heterogenous prescriptions. Nevertheless, the heterogeneous prescriptions of Method-2 to -4 can significantly ($p < 0.05$) escalate TCP for the cohort relative to Method-1 prescriptions.

The large variations between the distributions of cell density and tumor probability incorporated in Method-2 prescriptions and that incorporated in Method-4 prescriptions decreased the TCP of Method-2 prescriptions, as the Method-2 prescriptions were generated by over- and under-estimating expected tumor cell number of voxels. However, by including the patient-specific tumor probability via the TP (patient + atlas)-map, the precise information on expected tumor cell numbers can enable Method-3 prescriptions to yield a higher TCP level.

4.2.2 | Impact on individuals

If a population atlas of tumor cell characteristics is used to redistribute an otherwise uniformly-prescribed integral energy, it is expected that for a proportion of patients there will be a decrease in expected tumor control relative to that for the uniform prescription, rather than an increase. As examples of the TCP of Method-2 and -3 prescriptions close or distant to the TCP of Method-4 prescription, prescriptions of patient-02 and patient-07 were selected (Figure 6). The Method-2 and -3 prescriptions of patient-07 resulted in more underdosing (Figure 7b) than seen for patient-02 (Figure 7a). After mapping the CD- and TP-atlas back to each individual's prostate geometry by deformable registration, both the CD- and TP-atlas does not completely cover a patient's prostate, and naturally the uncovered voxels were labeled with 0 cell density and tumor probability. This is a limitation of the atlas which was created with axial histology sections and excluded the most inferior and superior parts of the prostate apex and base that were sectioned sagittally according to clinical protocols.[17] Consequently, if the volume was not encompassed by the atlas, then the optimizer could potentially underdose the volume, treating it as healthy tissue in Method-2 prescriptions or tumor with 0 cells in Method-3 prescriptions.

4.3 | Variations across prostate zones

As indicated by the patient-specific CD- and TP (patient + atlas)-map of the cohort, the peripheral zone (PZ) had a significantly larger expected tumor cell number than the non-peripheral zone (Mann–Whitney U rank test, $P = 0.003$). Previous studies have reported that IPLs are most commonly found in the PZ.[46–49] The posterior section of the prostate is where the peripheral zone is located, and for that section of the prostate, as expected there were significantly higher numbers of tumor cells than anterior section of the prostate (Mann–Whitney U rank test, $P = 5.7 \times 10^{-24}$). For posterior section of the prostate, the prescriptions of Method-2 to -4 achieved a significantly higher TCP than the Method-1 prescription (Table 4), since compared to the prescriptions of Method-2 to -4, this region is generally prescribed with lower doses by the homogenous dose prescriptions.

For the anterior section of the prostate apex and base, no significant differences were found between prescriptions of Method-2 to -4 and that of Method-1 for the cohort (Table 4). Those sub-sections had significantly lower (Mann–Whitney U rank test, $P = 7.3 \times 10^{-26}$) numbers of expected tumor cells than other sections, and the Method-1 prescriptions achieved higher TCPs by prescribing higher doses than prescriptions of Method-2 to -4 to those regions.

4.4 | Similar studies

Except for cell density and tumor probability, voxel-wise prescriptions for the prostate can be generated using other imaging or biological features. Using a TCP model[50,51] that incorporated voxel-wise ^{18}F-choline PET imaging, Dirscherl et al.[52] generated an optimal

prostate dose prescription by reaching the voxel-wise dose distribution with the largest calculated TCP. Similarly, by incorporating GS in a TCP model and maximizing TCP, Grönlund et al.[53] generated optimal dose prescriptions using prostate GS distributions derived from the distributions of apparent diffusion coefficients (ADC).[54,55] The prescription can also be generated by a spatial map of tumor hypoxia, by incorporating the scored voxel-level risk of hypoxia derived from mpMRI,[56] Using these spatial maps, Her et al. generated five IMRT plans and demonstrated the ability to greatly mitigate the effects of hypoxia.[57]

When voxel-wise data of biological features are not available, the energy to be delivered to the prostate can be redistributed by prescribing higher or lower doses to one lobe of the prostate. By defining the involved lobe with biopsies, Amini et al.[58] prescribed 70 and 50.4 Gy in 28 fractions to the involved and uninvolved lobes, respectively.

The dose redistribution can also be achieved by dose escalation to the detected IPLs. Boosting IPLs without violating the dose constrains of OARs has been shown to be feasible,[59-61] and an increased tumor control relative to uniform dose prescription has been reported.[38] However, the undetected lesions or the uncertainty in delineating IPLs from MRI or PET images[62] may lead to underdosing of sub-volumes of the prostate. Such a problem can be improved by applying the suggested prostate dose redistribution by the CD- and TP-atlases to cover the potential tumor location as derived from a patient population.

To generate treatment plans in a treatment planning system (TPS) using the voxel-wise dose prescription with the best expected treatment outcome, studies have utilized minimization of difference between each voxel dose and the prescribed dose as the main objective.[52,63] However, as previously discussed, a lower mean underdosing of a planned dose distribution to the prescribed dose distribution may not lead to higher TCP. Hence, rather than aiming to duplicate the prescribed dose distribution on a TPS, TCP-based plan optimization should be considered. In the work of Her et al.,[14] treatment plans were optimized in an experimental TPS (MatRad[64,65]) using an objective of maximizing TCP.

4.5 | Future work

By analyzing the cell density distribution obtained from histology images, Reynolds et al.[19] reported that the cell densities of tumors are significantly different to those of healthy prostate tissue (Kolmogorov–Smirnov tests, $p < 0.05$), which suggested that the tumor volumes detected by histology data were expected to have higher cell densities. However, the CD-atlas used in Method-3 prescriptions only provided the voxel-wise cell density values summarized from the investigated cohort—it cannot predict the cell density distribution according to the patient-specific tumor probability distribution. A model predicting cell density from prostate MRI features was developed by Sun et al.[16] In future work, the tumor probability distribution can be added as one of the features to better predict cell density distribution, and the model can be used in Method-3 prescriptions to further escalate the TCP level.

It should be noted that this work has not considered changes in tumor characteristics throughout treatment. Accounting for such change would require intra-fraction assessment of the tumor characteristics, potentially via a linac-incorporated MRI and application of a predictive model based on MR image features. It should also be noted that the present work has not considered the distribution of oxygenation within the prostate—incorporating radio-resistance due to tumor hypoxia[66-68] may alter the resulting redistributed dose distribution. The suggested future work includes integrating the oxygenation distributions of individuals in the cohort and incorporating oxygen enhancement ratio (OER) into the TCP model[69-72] for optimal heterogeneous dose prescription generation.

The 63-patient cohort used in this research should not be considered as an accurate representation of the broader population, though practical limitations required this assumption in this work. Ideally, comparison of use of population versus individual tumor characteristics would be performed using individuals from outside the population. Including a larger cohort would generate a more robust and representative representation of cell density and tumor probability atlases. However, patients selected for radical prostatectomy generally have lower risk features and therefore expanding the cohort to include those with high-risk features could be challenging.

For commercial TPSs that do not accept voxel-wise dose prescription as planning objectives, efforts are needed to convert the generated optimal heterogenous prescriptions in this research into structure-based dose prescriptions. In the studies of Deveau et al.[73] and Flynn et al.,[74] voxel-based dose prescriptions were discretized into serval equally sized dose bins. The resulting structures were then prescribed to the corresponding average bin dose. Nonetheless, in comparison to voxel-based dose prescription, the resulting dose distribution of generated structure-based dose prescriptions would naturally have reduced heterogeneity and thus a decreased tumor control. Therefore, to generate structure-based dose prescriptions with the maximal TCP, a new route from voxel-wise dose prescriptions to structure-based prescriptions needs to be established by incorporating the distribution of tumor characteristics. This is the topic of ongoing work.

Finally, this work only represents the voxel-wise prescription generation prior to treatment planning and delivery. No impact of the treatment planning

system, physical limitations of dose delivery or patient-related factors have been included. Work is ongoing to determine the deliverability of derived heterogeneous prescriptions across delivery technologies, as well as methods to ensure their robustness to uncertainties.

4.6 | Conclusion

This work has demonstrated the potential benefit for tumor control by redistributing escalated doses. With four different methods that utilized the distribution of biological features from different resources, the optimal dose prescriptions were generated for a cohort of 63 patients by increasing the calculated prostate TCP under the same integral energy level for four fractionation schedules. Relative to a conventional homogenous dose prescription, the generated optimal heterogeneous dose prescriptions can escalate tumor control for most patients. The fractionation schedule that benefited the most from optimal heterogeneous dose prescriptions was CF.

In a typical scenario, where patient-specific histology information is not available and where the population-based distribution of biological features is used (Method-2), the heterogeneous dose prescriptions generated a higher TCP for at least 87% of patients in EH and MH compared to a conventional homogenous prescription (Method-1). By integrating additional patient-specific tumor probability distributions (Method-3), heterogeneous prescriptions could further escalate the TCP level for the cohort. Dose redistribution via prescriptions based on patient-specific histology information (Method-4) demonstrated the voxel-wise dose distribution that could achieve the upper theoretical limit of tumor control.

ACKNOWLEDGMENTS

The authors have nothing to report.

Open access publishing facilitated by The University of Western Australia, as part of the Wiley - The University of Western Australia agreement via the Council of Australian University Librarians.

CONFLICT OF INTEREST STATEMENT

The authors declare no conflicts of interest.

ORCID

Yutong Zhao https://orcid.org/0000-0001-6477-0205

REFERENCES

1. Kuban DA, Tucker SL, Dong L, et al. Long-term results of the MD Anderson randomized dose-escalation trial for prostate cancer. *Int J Radiat Oncol Biol Phys*. 2008;70(1):67-74.
2. Creak A, Hall E, Horwich A, et al. Randomised pilot study of dose escalation using conformal radiotherapy in prostate cancer: long-term follow-up. *Br J Cancer*. 2013;109(3):651-657.
3. Zietman AL, Bae K, Slater JD, et al. Randomized trial comparing conventional-dose with high-dose conformal radiation therapy in early-stage adenocarcinoma of the prostate: long-term results from proton radiation oncology group/american college of radiology 95-09. *J Clin Oncol*. 2010;28(7):1106.
4. Beckendorf V, Guerif S, Le Prisé E, et al. 70 Gy versus 80 Gy in localized prostate cancer: 5-year results of GETUG 06 randomized trial. *Int J Radiat Oncol Biol Phys*. 2011;80(4):1056-1063.
5. Heemsbergen WD, Al-Mamgani A, Slot A, Dielwart MFH, Lebesque JV. Long-term results of the Dutch randomized prostate cancer trial: impact of dose-escalation on local, biochemical, clinical failure, and survival. *Radiother Oncol*. 2014;110(1):104-109.
6. Zelefsky MJ, Yamada Y, Fuks Z, et al. Long-term results of conformal radiotherapy for prostate cancer: impact of dose escalation on biochemical tumor control and distant metastases-free survival outcomes. *Int J Radiat Oncol Biol Phys*. 2008;71(4):1028-1033.
7. Zelefsky MJ, Pei X, Chou JF, et al. Dose escalation for prostate cancer radiotherapy: predictors of long-term biochemical tumor control and distant metastases–free survival outcomes. *Eur Urol*. 2011;60(6):1133-1139.
8. Pahlajani N, Ruth KJ, Buyyounouski MK, et al. Radiotherapy doses of 80 Gy and higher are associated with lower mortality in men with Gleason score 8 to 10 prostate cancer. *Int J Radiat Oncol Biol Phys*. 2012;82(5):1949-1956.
9. Kang J-K, Cho CK, Choi CW, et al. Image-guided stereotactic body radiation therapy for localized prostate cancer. *Tumori J*. 2011;97(1):43-48.
10. Oliai C, Lanciano R, Sprandio B, et al. Stereotactic body radiation therapy for the primary treatment of localized prostate cancer. *J Radiat Oncol*. 2013;2(1):63-70.
11. Bernetich M, Oliai C, Lanciano R, et al. SBRT for the primary treatment of localized prostate cancer: the effect of Gleason score, dose and heterogeneity of intermediate risk on outcome utilizing 2.2014 NCCN risk stratification guidelines. *Front Oncol*. 2014;4:312.
12. Dearnaley D, Syndikus I, Mossop H, et al. Conventional versus hypofractionated high-dose intensity-modulated radiotherapy for prostate cancer: 5-year outcomes of the randomised, non-inferiority, phase 3 CHHiP trial. *Lancet Oncol*. 2016;17(8):1047-1060.
13. Kountouri M, Zilli T, Rouzaud M, et al. Moderate hypofractionated protracted radiation therapy and dose escalation for prostate cancer: do dose and overall treatment time matter? *Int J Radiat Oncol Biol Phys*. 2016;94(2):272-279.
14. Her EJ, Haworth A, Reynolds HM, et al. Voxel-level biological optimisation of prostate IMRT using patient-specific tumour location and clonogen density derived from mpMRI. *Radiat Oncol*. 2020;15(1):1-13.
15. Zhao Y, Haworth A, Reynolds HM, et al. Patient-specific voxel-level dose prescription for prostate cancer radiotherapy considering tumour cell density and grade distribution. *Med Phys*. 2023:3746-3761.
16. Sun Yu, Reynolds HM, Wraith D, et al. Voxel-wise prostate cell density prediction using multiparametric magnetic resonance imaging and machine learning. *Acta Oncol (Madr)*. 2018;57(11):1540-1546.
17. Finnegan RN, Reynolds HM, Ebert MA, et al. A statistical, voxelised model of prostate cancer for biologically optimised radiotherapy. *Phys Imaging Radiat Oncol*. 2022;21:136-145.
18. Reynolds HM, Williams S, Zhang A. Development of a registration framework to validate MRI with histology for prostate focal therapy. *Med Phys*. 2015;42(12):7078-7089.
19. Reynolds HM, Williams S, Zhang AM, et al. Cell density in prostate histopathology images as a measure of tumor distribution. Medical Imaging 2014: Digital Pathology. International Society for Optics and Photonics; 2014.

20. Wang JZ, Guerrero M, Li XA. How low is the α/β ratio for prostate cancer? *Int J Radiat Oncol Biol Phys*. 2003;55(1):194-203.
21. Haworth A, Ebert M, Waterhouse D, Joseph D, Duchesne G. Prostate implant evaluation using tumour control probability—the effect of input parameters. *Phys Med Biol*. 2004;49(16):3649.
22. Her EJ, Haworth A, Rowshanfarzad P, Ebert MA. Progress towards patient-specific, spatially-continuous radiobiological dose prescription and planning in prostate cancer IMRT: an overview. *Cancers*. 2020;12(4):854.
23. Shusharina N, Craft D, Chen YL, Shih H, Bortfeld T. The clinical target distribution: a probabilistic alternative to the clinical target volume. *Phys Med Biol*. 2018;63(15):155001.
24. Bortfeld T, Shusharina N, Craft D. Probabilistic definition of the clinical target volume—implications for tumor control probability modeling and optimization. *Phys Med Biol*. 2021;66(1):01NT01.
25. Keall P, Webb S. Optimum parameters in a model for tumour control probability, including interpatient heterogeneity: evaluation of the log-normal distribution. *Phys Med Biol*. 2006;52(1):291.
26. Draulans C, Van Der Heide UA, Haustermans K, et al. Primary endpoint analysis of the multicentre phase II hypo-FLAME trial for intermediate and high risk prostate cancer. *Radiother Oncol*. 2020;147:92-98.
27. Koskela K, Palmgren J-E, Heikkilä J, et al. Hypofractionated stereotactic body radiotherapy for localized prostate cancer–first Nordic clinical experience. *Acta Oncol (Madr)*. 2017;56(7):978-983.
28. Zelefsky MJ, Cowen D, Fuks Z, et al. Long term tolerance of high dose three-dimensional conformal radiotherapy in patients with localized prostate carcinoma. *Cancer*. 1999;85(11):2460-2468.
29. Katz A, Kang J. Stereotactic body radiotherapy with or without external beam radiation as treatment for organ confined high-risk prostate carcinoma: a six year study. *Radiat Oncol (London, England)*. 2014;9(1):1-1.
30. Alayed Y, Cheung P, Vesprini D, et al. SABR in high-risk prostate cancer: outcomes from 2 prospective clinical trials with and without elective nodal irradiation. *Int J Radiat Oncol Biol Phys*. 2019;104(1):36-41.
31. Rana Z, Hong RL, Abugideiri M, et al. Sexual, irritative, and voiding outcomes, following stereotactic body radiation therapy for prostate cancer. *Radiat Oncol*. 2015;10(1):1-9.
32. Freeman D, Dickerson G, Perman M. Multi-institutional registry for prostate cancer radiosurgery: a prospective observational clinical trial. *Front Oncol*. 2015;4:369.
33. Incrocci L, Wortel RC, Alemayehu WG, et al. Hypofractionated versus conventionally fractionated radiotherapy for patients with localised prostate cancer (HYPRO): final efficacy results from a randomised, multicentre, open-label, phase 3 trial. *Lancet Oncol*. 2016;17(8):1061-1069.
34. Wang S-C, Ting W-C, Chang Y-C, et al. Whole pelvic radiotherapy with stereotactic body radiotherapy boost vs. conventionally fractionated radiotherapy for patients with high or very high-risk prostate cancer. *Front Oncol*. 2020;10:814.
35. Kim HJ, Phak JH, Kim WC. Clinical outcomes of whole pelvis radiotherapy and stereotactic body radiotherapy boost for intermediate-and high-risk prostate cancer. *Asia Pac J Clin Oncol*. 2017;13(5):e342-e347.
36. Lin Yu-W, Lin Li-C, Lin K-Li. The early result of whole pelvic radiotherapy and stereotactic body radiotherapy boost for high-risk localized prostate cancer. *Front Oncol*. 2014;4:278.
37. Lips IM, Van Der Heide UA, Haustermans K, et al. Single blind randomized phase III trial to investigate the benefit of a focal lesion ablative microboost in prostate cancer (FLAME-trial): study protocol for a randomized controlled trial. *Trials*. 2011;12(1):1-11.
38. Kerkmeijer LGW, Groen VH, Pos FJ, et al. Focal boost to the intraprostatic tumor in external beam radiotherapy for patients with localized prostate cancer: results from the FLAME Randomized Phase III Trial. *J Clin Oncol*. 2021:787-796. JCO. 20.02873.
39. Oermann EK, Slack RS, Hanscom HN, et al. A pilot study of intensity modulated radiation therapy with hypofractionated stereotactic body radiation therapy (SBRT) boost in the treatment of intermediate-to high-risk prostate cancer. *Technol Cancer Res Treat*. 2010;9(5):453-462.
40. Mercado C, Kress M-A, Cyr RA, et al. Intensity-modulated radiation therapy with stereotactic body radiation therapy boost for unfavorable prostate cancer: the Georgetown University experience. *Front Oncol*. 2016;6:114.
41. Storn R, Price K. Differential evolution–a simple and efficient heuristic for global optimization over continuous spaces. *J Global Optim*. 1997;11(4):341-359.
42. Storn R. On the usage of differential evolution for function optimization. Proceedings of north american fuzzy information processing. Ieee; 1996.
43. Virtanen P, Gommers R, Oliphant TE, et al. SciPy 1.0: fundamental algorithms for scientific computing in Python. *Nat Methods*. 2020;17(3):261-272.
44. Freedman D, Pisani R, Purves R, Adhikari A. *Statistics*. WW Norton & Company New York; 2007.
45. Rodgers JL, Nicewander WA. Thirteen ways to look at the correlation coefficient. *Am Stat*. 1988;42(1):59-66.
46. Nutting CM, Corbishley CM, Sanchez-Nieto B, Cosgrove VP, Webb S, Dearnaley DP. Potential improvements in the therapeutic ratio of prostate cancer irradiation: dose escalation of pathologically identified tumour nodules using intensity modulated radiotherapy. *Br J Radiol*. 2002;75(890):151-161.
47. Van Lin ENJT, Fütterer JJ, Heijmink SWTPJ, et al. IMRT boost dose planning on dominant intraprostatic lesions: gold marker-based three-dimensional fusion of CT with dynamic contrast-enhanced and 1H-spectroscopic MRI. *Int J Radiat Oncol Biol Phys*. 2006;65(1):291-303.
48. Kim Y, Hsu I-CJ, Lessard E, Kurhanewicz J, Noworolski SM, Pouliot J. Class solution in inverse planned HDR prostate brachytherapy for dose escalation of DIL defined by combined MRI/MRSI. *Radiother Oncol*. 2008;88(1):148-155.
49. Tamihardja J, Zenk M, Flentje M. MRI-guided localization of the dominant intraprostatic lesion and dose analysis of volumetric modulated arc therapy planning for prostate cancer. *Strahlenther Onkol*. 2018;195(2):145-152.
50. Yang Y, Xing L. Towards biologically conformal radiation therapy (BCRT): selective IMRT dose escalation under the guidance of spatial biology distribution. *Med Phys*. 2005;32(6):1473-1484. Part1.
51. Rickhey M, Bogner L. Optimizing tumor control probability, assuming a heterogeneous distribution of radiobiological properties for glioblastoma. *Int J Radiat Oncol Biol Phys*. 2008;72(1):S533-S534.
52. Dirscherl T, Rickhey M, Bogner L. Feasibility of TCP-based dose painting by numbers applied to a prostate case with 18F-choline PET imaging. *Zeitschrift für Medizinische Physik*. 2012;22(1):48-57.
53. Grönlund E, Almhagen E, Johansson S, et al. Robust treatment planning of dose painting for prostate cancer based on ADC-to-Gleason score mappings–what is the potential to increase the tumor control probability? *Acta Oncol (Madr)*. 2020:1-8.
54. Turkbey B, Shah VP, Pang Y, et al. Is apparent diffusion coefficient associated with clinical risk scores for prostate cancers that are visible on 3-T MR images? *Radiology*. 2011;258(2):488-495.
55. Grönlund E, Johansson S, Nyholm T, Thellenberg C, Ahnesjö A. Dose painting of prostate cancer based on Gleason score correlations with apparent diffusion coefficients. *Acta Oncol (Madr)*. 2018;57(5):574-581.
56. Sun Yu, Williams S, Byrne D, et al. Association analysis between quantitative MRI features and hypoxia-related genetic profiles in prostate cancer: a pilot study. *Br J Radiol*. 2019;92(1104):20190373.

57. Her EJ, Haworth A, Sun Yu, et al. Biologically targeted radiation therapy: incorporating patient-specific hypoxia data derived from quantitative magnetic resonance imaging. *Cancers*. 2021;13(19):4897.
58. Amini A, Westerly DC, Waxweiler TV, Ryan N, Raben D. Dose painting to treat single-lobe prostate cancer with hypofractionated high-dose radiation using targeted external beam radiation: is it feasible? *Med Dosim*. 2015;40(3):256-261.
59. Onjukka E, Uzan J, Baker C, Howard L, Nahum A, Syndikus I. Twenty fraction prostate radiotherapy with intra-prostatic boost: results of a pilot study. *Clin Oncol*. 2017;29(1):6-14.
60. Alayed Y, Davidson M, Liu S, et al. Evaluating the tolerability of a simultaneous focal boost to the gross tumor in prostate SABR: a toxicity and quality-of-life comparison of two prospective trials. *Int J Radiat Oncol Biol Phys*. 2020;107(1):136-142.
61. Blake SW, Stapleton A, Brown A, et al. A study of the clinical, treatment planning and dosimetric feasibility of dose painting in external beam radiotherapy of prostate cancer. *Phys Imaging Radiat Oncol*. 2020;15:66-71.
62. Zamboglou C, Thomann B, Koubar K, et al. Focal dose escalation for prostate cancer using 68Ga-HBED-CC PSMA PET/CT and MRI: a planning study based on histology reference. *Radiat Oncol (London, England)*. 2018;13(1):81-81.
63. Van Schie MA, Steenbergen P, Dinh CV, et al. Repeatability of dose painting by numbers treatment planning in prostate cancer radiotherapy based on multiparametric magnetic resonance imaging. *Phys Med Biol*. 2017;62(14):5575.
64. Wieser H-P, Cisternas E, Wahl N, et al. Development of the open-source dose calculation and optimization toolkit matRad. *Med Phys*. 2017;44(6):2556-2568.
65. Cisternas E, Mairani A, Ziegenhein P, Jakel O, Bangert M. matRad-a multi-modality open source 3D treatment planning toolkit. World Congress on Medical Physics and Biomedical Engineering, June 7–12, 2015, Toronto, Canada. Springer; 2015.
66. Dhani N, Fyles A, Hedley D, Milosevic M. The clinical significance of hypoxia in human cancers. *Seminars in Nuclear Medicine*. Elsevier; 2015.
67. Hill RP, Bristow RG, Fyles A, Koritzinsky M, Milosevic M, Wouters BG. Hypoxia and predicting radiation response. *Seminars in Radiation Oncology*. Elsevier; 2015.
68. Muz B, De La Puente P, Azab F, Azab AK. The role of hypoxia in cancer progression, angiogenesis, metastasis, and resistance to therapy. *Hypoxia*. 2015;3:83.
69. Wenzl T, Wilkens JJ. Modelling of the oxygen enhancement ratio for ion beam radiation therapy. *Phys Med Biol*. 2011;56(11):3251.
70. Wenzl T, Wilkens JJ. Theoretical analysis of the dose dependence of the oxygen enhancement ratio and its relevance for clinical applications. *Radiat Oncol*. 2011;6(1):1-9.
71. Strigari L, Torriani F, Manganaro L, et al. Tumour control in ion beam radiotherapy with different ions in the presence of hypoxia: an oxygen enhancement ratio model based on the microdosimetric kinetic model. *Phys Med Biol*. 2018;63(6):065012.
72. Søvik Å, Malinen E, Bruland ØS, Bentzen SM, Olsen DR. Optimization of tumour control probability in hypoxic tumours by radiation dose redistribution: a modelling study. *Phys Med Biol*. 2006;52(2):499.
73. Deveau MA, Bowen SR, Westerly DC, Jeraj R. Feasibility and sensitivity study of helical tomotherapy for dose painting plans. *Acta Oncol (Madr)*. 2010;49(7):991-996.
74. Flynn RT, Bowen SR, Bentzen SM, Rockwell Mackie T, Jeraj R. Intensity-modulated x-ray (IMXT) versus proton (IMPT) therapy for theragnostic hypoxia-based dose painting. *Phys Med Biol*. 2008;53(15):4153.

How to cite this article: Zhao Y, Haworth A, Reynolds HM, et al. Towards optimal heterogeneous prostate radiotherapy dose prescriptions based on patient-specific or population-based biological features. *Med Phys*. 2024;1-16. https://doi.org/10.1002/mp.16936